### ARTICLE

Check for updates

# Active optomechanics

Deshui Yu [1✉] & Frank Vollmer [1✉]

Cavity optomechanics explores the coupling between optical and mechanical modes mediated by the radiation pressure force. Unlike the passive scheme, the active optomechanics with optical gain directly imposes the mechanical motion upon the lasing dynamics, unveiling the intrinsic properties determined by the system itself. Here we numerically explore the general characteristics of the active optomechanics. The effects of the mechanical oscillation on the macroscopic laser include introducing multiple unstable regimes in the lasing phase, shifting the laser central frequency, broadening the laser spectrum, and degrading the laser frequency stability. Reducing the optical gain down to one active atom highlights the quantum nature of atom–cavity and photon–phonon interactions. The one-atom optomechanical microlaser does not only emit nonclassical photons but also generate nonclassical photon–phonon pairs. Our work extends the cavity optomechanics to the active fashion, paving the way towards optomechanical light sources for photonic integrated circuits, on-chip quantum communication, and biosensing.

[1] Living Systems Institute, Physics and Astronomy, University of Exeter, Exeter, UK. ✉email: d.d.yu@exeter.ac.uk; f.vollmer@exeter.ac.uk

The parametric coupling between optical and mechanical degrees of freedom originates from the light momentum transfer to the mechanical objects that are located inside the optical cavities[1] and is usually modelled as the spring–mass oscillators. Various motivations are driving the vastly growing interest in cavity optomechanics[2,3] and a great variety of opto-mechanical devices have been developed, including suspended macroscopic/microscopic mirrors[4–6], micropillars[7], membranes[8], whispering-gallery-mode microcavities[9–12], and nanorods[13]. The retarded nature of the radiation pressure force allows for suppressing[11]/pumping[14] the mechanical vibration through controlling the incident light. In particular, the optomechanical coupling in the resolved-sideband limit (i.e. the mechanical oscillation frequency greatly exceeds the cavity loss rate) enables cooling of mechanical vibration to the quantum-mechanical ground state[10,15], leading to the ultrasensitive mass/displacement/force transduction[16–18]. In single-molecule detection, employing the optomechanical effect boosts the sensing resolution by the quality factor of the mechanical mode compared to the conventional methods[19]. In nonequilibrium thermodynamics, an opto-mechanical array mediated by cavity field allows for monitoring the heat transport in real time[20]. Additionally, hybridizing optomechanical systems with lattice-confined ultracold atoms enables the spatial modulation of atomic density[21] and the manipulation of the motion of atoms[22]. Quantum states can be also transferred between optical and mechanical modes in a coherent fashion (i.e. the optomechanical-coupling strength well exceeds both optical and mechanical decoherence rates[9]) by using modern quantum optical techniques[9]. Furthermore, the opto-mechanical coupling may lead to a stationary entanglement between an optical cavity mode and a macroscopic vibrating mirror[23].

Numerous studies have been focused on the cavity opto-mechanical systems that are operated in a passive manner[3]. In such setups, an optical cavity is pumped by an external laser beam whose central frequency is detuned from the resonance frequency of the cavity mode. The optomechanical coupling is simply tuned by changing the intensity and frequency of the input laser. The mechanical vibration is mapped onto the optical phase of the intracavity field and the transmission spectrum of the cavity is monitored. The noise spectrum of the mechanical displacement can be attained by using conventional methods, such as balanced homodyne detection[24], Hänsch–Coulliaud polarization spectroscopy[25], and Pound–Drever–Hall technique[26]. Nevertheless, the optical phase measurement suffers from unavoidable technical noise sources that are associated with intensity and phase fluctuations in probe laser and local oscillator. Addressing these issues requires extra frequency and polarization stabilization steps and associated optical and electrical components[27], complicating the design of optomechanical systems. In addition, the limited tuning speed and range of the probe laser frequency impede the detection of high-frequency mechanical vibration.

Recently, the active cavity optomechanics[28], also known as optomechanical lasing, has drawn much attention. In this new configuration, a spring–mass oscillator is mounted onto one end mirror of a laser cavity. The gain particle–photon and photon–phonon interactions interfere with each other, tran-scribing the mechanical oscillation directly onto the lasing dynamics[29]. Up to now, the active optomechanical scheme has been implemented only on the vertical-external-cavity surface-emitting laser with an ultralight-weight mirror[29–32]. The results manifest a substantially enhanced photon–phonon interaction[32] and a high-speed wide-range wavelength sweep[31]. In comparison to the passive operation fashion, the active optomechanics holds the advantages of simple system structures (i.e. no need for extra frequency and intensity stabilization procedures or associated

optical and electrical components), revealing the intrinsic optical properties (i.e. frequency shift, spectral broadening, temporal coherence, and photon statistics) that are entirely determined by an optomechanical system itself, and the potential role of wavelength-tunable light sources in nanophotonic integrated circuits[30]. Nevertheless, the previous demonstrations[29–32] have been less focused on the effects of the mechanical oscillation on the optical properties of the lasing dynamics.

In addition, thus far, research has been carried out mainly on the optomechanical coupling between a classical optical mode and a mechanical oscillation mode that may be modelled as either a classical spring–mass or a quantum harmonic oscillator with particle-like excitations, known as phonons. By contrast, less attention has been given to the cavity optomechanical systems with small amounts of light quanta (photons) and pho-nons. In this limit, the quantum nature of light plays a key role in its interaction with the mechanical oscillator and the full quan-tum treatment should be applied to analyze the cavity optomechanics[33]. The resultant optomechanical microlasers potentially act as nonclassical light sources that are of particular importance to quantum communication and computing.

In this paper, we numerically investigate the active opto-mechanics where a macroscopic/microscopic lasing dynamics is coupled to a mechanical oscillator. For the macroscopic system composed of an optical cavity interacting with an ensemble of active atoms, the mechanical oscillation induces multiple unstable steady-state regimes in the lasing phase, broadening the power spectral density compared to the corresponding conventional laser system, and degrading the laser frequency stability. In the microscopic limit, the one-atom optomechanical microlaser emits nonclassical photons, the dependence of which on the atom–cavity detuning exhibits multiple submaxima because of the strong photon–phonon interface. The spectrum and photon statistics of the optomechanical microlaser also differ much from that of the common one-atom microlaser. Interestingly, the cross-correlation function between photons and phonons shows a nonclassical behaviour of the photon–phonon pair generation. To our best knowledge, such a one-atom optomechanical microlaser has not been studied yet and may operate as a nonclassical light source, whose optical properties can be tuned by controlling the mechanical oscillator, for quantum networking. The recent microcavity and nanophotonic technologies allow for testing the predictions obtained in this study.

## Results

**Physical model**. We restrict our attention to the simplest cavity optomechanics, where one optical mode interacts with one mechanical mode. Figure 1a illustrates a generic scheme of the active optomechanical system. An ensemble of atoms is located inside an optical cavity that is composed of a fixed and movable mirror. The movable mirror undergoes a one-dimensional har-monic oscillation $x(t)$ at a radio frequency $\Omega$. The damping rate of the mechanical vibration is $\Gamma$ with the corresponding quality factor $Q_{\mathrm{m}} = \Omega/\Gamma$. The optical cavity has a resonance frequency $\omega_{\mathrm{C}}$ when $x = 0$. The cavity loss rate is $\kappa$ with the corresponding quality factor $Q = \omega_{\mathrm{C}}/\kappa$. To the linear approximation, the non-zero mechanical displacement $x \neq 0$ introduces a frequency shift $\delta(t) = \xi x(t)$ to the optical cavity mode. The frequency pull parameter $\xi$ takes the form $\xi = -\omega_{\mathrm{C}}/L$ for a Fabry–Pérot-type cavity with a length $L$ and $\xi = -\omega_{\mathrm{C}}/R_{\mathrm{WGM}}$ for the fundamental mode in a whispering-gallery-mode microcavity with a radius $R_{\mathrm{WGM}}$. The zero-point fluctuation of the mechanical oscillator is defined as $x_{\mathrm{ZPF}} = \sqrt{\hbar/2m_{\mathrm{eff}}\Omega}$, where the effective mass $m_{\mathrm{eff}}$ depends on the specific mode under consideration and the choice of the normalized displacement[34]. The atoms play the role of the
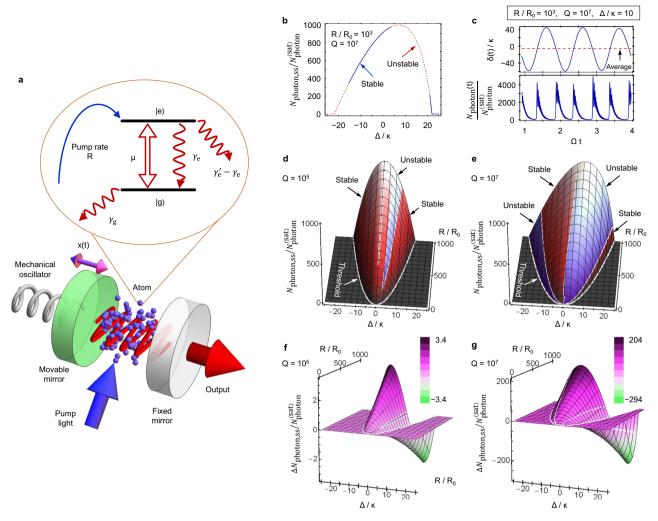
**Fig. 1 Active optomechanics in the macroscopic limit. a** Schematic of a generic cavity optomechanical system that operates in an active fashion. An ensemble of two-level (upper $|e\rangle$ and lower $|g\rangle$) atoms is coupled to an optical cavity with a single-photon coupling strength $\mu$. A pump light excites the atoms onto $|e\rangle$ at a rate $R$. The total decay rate of $|e\rangle$ is $\gamma_e'$, wherein the decay rate of the atom from $|g\rangle$ to $|e\rangle$ is $\gamma_e$. The fast decay rate $\gamma_g$ of $|g\rangle$ ensures the population inversion between $|e\rangle$ and $|g\rangle$. The active atoms emit photons into the optical cavity. The position of one cavity mirror is fixed while the other mirror is movable. The motion of the movable mirror is modelled as a mechanical oscillator with a displacement $x(t)$, oscillation frequency $\Omega$, and damping rate $\Gamma$. The radiation pressure of the intracavity field drives the mechanical oscillator. **b** Steady-state photon number $N_{photon,ss}$ (in units of the saturation photon number $N_{photon}^{(sat)}$) as a function of the detuning $\Delta = \omega_C - \omega_A$ between the cavity mode frequency $\omega_C$ and the atomic transition frequency $\omega_A$. The pump rate is set at $R = 10^3 R_0$ with the minimum pump threshold $R_0$ and the cavity quality factor is $Q = 10^7$. The cavity loss rate $\kappa = \omega_C/Q$ is chosen as the frequency unit in the plot. The solid curves denote the stable steady-state solutions while the dashed lines correspond to the unstable steady-state solutions. **c** Time evolutions of the mechanical-displacement-induced detuning $\delta(t)$ and the intracavity photon number $N_{photon}(t)$ for the optomechanical system operating at an unstable steady state. The dashed line corresponds to the average value of $\delta(t)$. **d, e** Dependences of the steady-state $N_{photon,ss}$ on the detuning $\Delta$ and the pump rate $R$ for $Q = 10^5$ and $Q = 10^7$, respectively. The boundaries of unstable steady-state regions have been plotted. The red shading denotes the stable steady states while the blue shading corresponds to the unstable steady states. **f, g** Photon differences $\Delta N_{photon,ss}$ between the active optomechanical system and the corresponding conventional laser for $Q = 10^5$ and $Q = 10^7$, respectively.

source of the intracavity field $E(t) = \sqrt{\hbar\omega_C/2\varepsilon_0 V_{eff}}\, a(t)$ with the reduced Planck's constant $\hbar$, the vacuum electric permittivity $\varepsilon_0$, the effective volume $V_{eff}$ of the cavity mode, and the dimensionless amplitude $a(t)$. Each atom is modelled as a two-level system, i.e. upper $|e\rangle$ and lower $|g\rangle$ states, with a transition frequency $\omega_A$. The cavity mode frequency $\omega_C$ is close to $\omega_A$ with a detuning $\Delta = \omega_C - \omega_A$. The total decay rate of $|e\rangle$ is $\gamma_e'$, wherein the amount corresponding to the $|g\rangle$-$|e\rangle$ branch is $\gamma_e$. The decay rate $\gamma_g$ of $|g\rangle$ should be larger than $\gamma_e$ for achieving the population inversion. The decay rate of the atomic polarization is then given by $\gamma_{eg} = (\gamma_e + \gamma_g)/2$. The coupling strength between the optical cavity and the atomic $|g\rangle$-$|e\rangle$ transition is $\mu = d\sqrt{\omega_C/2\varepsilon_0\hbar V_{eff}}$ with the associated electric dipole moment $d$ of the atom. The

atoms are continuously pumped into the upper $|e\rangle$ state at a rate $R$. The lasing action occurs for a large enough $R$. The radiation pressure force $F_{rad}(t) = -\hbar\xi N_{photon}(t)$ exerted on the movable mirror leads to the parametric coupling between optical and mechanical degrees of freedom of the cavity. Here, $N_{photon}(t) = |a(t)|^2$ accounts for the intracavity photon number.

The generic scheme described in Fig. 1a is actually a four-level optomechanical laser, which is feasible by means of current atomic and photonic technologies, for instances, active optical clocks with gaseous alkali-metal atoms[35,36] and whispering-gallery-mode microresonators doped by rare-earth ions[37,38] and organic molecules[39,40]. In what follows, we take neutral caesium atoms, whose external motion and internal states can be

manipulated and controlled at a high degree of precision by using laser beams in experiments[41], as the intracavity gain medium with the laser transition between $|e\rangle \equiv (5p^67s)\ ^2S_{1/2}$ and $|g\rangle \equiv (5p^66p)\ ^2P_{3/2}$ (Supplementary Note 1). The transition frequency is $\omega_A = 2\pi \times 204$ THz (wavelength of 1470 nm) and the relevant decay rates[42] are $\gamma_e = 2\pi \times 1.8$ MHz, $\gamma'_e = 2\pi \times 2.8$ MHz, $\gamma_g = 2\pi \times 5.2$ MHz, and $\gamma_{eg} = 2\pi \times 4.0$ MHz. A pump laser at 455 nm continuously drives the atoms from the ground $(5p^66s)\ ^2S_{1/2}$ to the excited $(5p^67p)\ ^2P_{3/2}$ state. The atoms are accumulated in $|e\rangle$ via the rapid decay from $(5p^67p)\ ^2P_{3/2}$ to $|e\rangle$ with the corresponding spontaneous emission rate of $2\pi \times 0.7$ MHz. The pump rate $R$ can be as high as $2\pi \times 13$ GHz for $2 \times 10^4$ atoms located inside the cavity. We further assume the cavity mode volume $V_{\rm eff}/(2\pi c/\omega_A)^3 = 2.5 \times 10^3$, which is experimentally feasible for various microcavities[43–45]. Here, $c$ denotes the speed of light in vacuum. The atom–cavity coupling strength is then computed as $\mu = 20\gamma_{eg}$.

The cavity $Q$ factor depends on the specific cavity structure. Fabry–Pérot[46] and whispering-gallery-mode[47] (micro)cavities may have an ultrahigh quality factor of the order of $10^{10}$. The corresponding photon loss rate $\kappa \sim 2\pi \times 20.4$ kHz is much smaller than the decay rate $\gamma_{eg}$ of the medium polarization. As a result, the laser system accesses the good-cavity regime with $\kappa \ll \gamma_{eg}$. In contrast, the attainable $Q$ factor of micropillar[48] and photonic crystal[49] microcavities is relatively low, ranging from $10^3$ to $10^6$, and thus the optomechanical laser operates in the bad-cavity limit with $\kappa \gg \gamma_{eg}$. Without losing the generality, we restrict ourselves to the range of $10^5 \leq Q \leq 10^7$ in this work. On the other hand, the vibrational frequency $\Omega$ and quality factor $Q_m$ of the mechanical oscillator also depend on the specific structure of the optical cavity, for examples, $\Omega/2\pi$ of $10 \sim 10^2$ MHz and $Q_m$ of $10^3$ for whispering-gallery-mode microcavities[11,27], $\Omega/2\pi$ of $10^{-2} \sim 10^2$ MHz and $Q_m$ of $10 \sim 10^4$ for cantilevers[50–52], and $\Omega/2\pi$ of $10^{-2} \sim 1$ MHz and $Q_m$ of $10^3$ for nanowires[53,54]. In this work, we study both macroscopic (i.e. atomic ensemble) and microscopic (i.e. one atom) active optomechanical systems. For the macroscopic optomechanics, without losing the generality, we choose $\Omega = 2\pi \times 10$ MHz and $Q_m = 10^2$ and hence the system stands outside the so-called sideband-resolved regime, i.e. $\kappa > \Omega$. We further assume the entire system is operated at the cryogenic temperature[55] $T = 1$ K. The average number of thermal photons approximates zero due to $k_B T/\hbar\omega_C \approx 0$ with the Boltzmann constant $k_B$. In contrast, the mechanical degree of freedom has a thermal occupation of $n_{\rm thrm} = 1/(e^{\hbar\Omega/k_B T} - 1) \approx 2083$, whose influence on the lasing dynamics is non-negligible. The assumption of cryogenic temperature facilitates the performance of the numerical simulation. For a higher $T$, for example, room temperature, $n_{\rm thrm}$ goes up strongly and the analysis presented below may be extended accordingly. For the microscopic optomechanics, in order to carry out the numerical simulation, we set $\Omega = 2\pi \times 100$ MHz, $Q_m = 10^2$ and the cryogenic temperature[56,57] $T = 10$ mK with $n_{\rm thrm} \approx 1.6$. Vastly reducing $n_{\rm thrm}$ is highly desirable because it highlights the quantum nature of phonons. In addition, to reveal the quantum behaviour of the photon–phonon interface, we set the cavity $Q$ factor at $10^7$ and as a result, the microscopic system accesses the sideband-resolved regime, i.e. $\kappa < \Omega$.

## Macroscopic optomechanics.
We first consider the macroscopic system with an optical cavity simultaneously interacting with a large number of active atoms and a classical mechanical oscillator. The light–matter interaction inside the cavity is described by a set of Heisenberg–Langevin equations while the mechanical

displacement $x(t)$ follows a second-order differential equation (i.e. spring–mass oscillator) driven by the radiation pressure force $F_{\rm rad}(t)$ (see Methods). It is worth noting that the macroscopic system may be also studied by using the density matrix method[58]. However, the huge dimension of the Hilbert space makes it challenging to perform the investigation, especially on the power spectral densities of the intracavity field and mechanical oscillation. In contrast, the Heisenberg–Langevin method strongly simplifies the mathematical modelling of the macroscopic system, allowing one to numerically simulate the lasing dynamics in an optomechanical cavity. In active optomechanics, the mechanical displacement $x(t)$ introduces an extra detuning $\delta(t)$ to the atom–cavity interaction, thereby affecting the intracavity photon number $N_{\rm photon}(t)$. This further changes the force $F_{\rm rad}(t)$ exerted on the movable mirror and in return affects $x(t)$. Thus, the optomechanical dynamics can be solved through a self-consistent method.

The system reaches the steady-state (denoted by the subscript ss) when the optical pump $R$ is balanced by the total energy loss experienced by the photons and atoms inside the cavity and the mechanical oscillator. The steady-state intracavity photon number is derived as (Supplementary Note 2)

$$N_{\rm photon,ss} \equiv \langle N_{\rm photon}(t \to \infty) \rangle = N_{\rm photon}^{\rm (sat)}\left(\frac{R}{R_0} - \frac{1}{\sin^2\varphi_{\rm ss}}\right), \quad (1)$$

with the saturation photon number $N_{\rm photon}^{\rm (sat)} = (\gamma_{eg}/2\mu^2)\gamma'_e\gamma_g/(\gamma'_e + \gamma_g - \gamma_e)$ and the minimum pump threshold $R_0 = (\gamma_{eg}/2\mu^2)\gamma'_e\gamma_g/(\gamma_g - \gamma_e)$. Here, $\langle \dots \rangle$ accounts for the expected value operation and $\varphi_{\rm ss}$ denotes the relative phase difference of the intracavity field with respect to the medium polarization. We have

$$\sin\varphi_{\rm ss} = -[1 + 4(\Delta + \delta_{\rm ss})^2/(\kappa + 2\gamma_{eg})^2]^{-1/2}, \quad (2)$$

with the steady-state mechanical-displacement-induced detuning $\delta_{\rm ss} \equiv \langle \delta(t \to \infty) \rangle = \xi x_{\rm ss} = -\delta_0 N_{\rm photon,ss} \leq 0$, $\delta_0 \equiv 2\delta_{\rm ZPF}^2/\Omega$, and the zero-point-fluctuation-induced detuning $\delta_{\rm ZPF} \equiv \xi x_{\rm ZPF}$. It is seen that the steady-state mechanical displacement $x_{\rm ss} \equiv \langle x(t \to \infty) \rangle = -(\delta_0/\xi)N_{\rm photon,ss}$ is positive and proportional to the photon number $N_{\rm photon,ss}$. Equation (1) is actually a quadratic equation with the variable $N_{\rm photon,ss}$ and only one solution is physically acceptable for the system parameters chosen in this work. Setting $\delta_{\rm ss} = 0$ in Eq. (2), one obtains a conventional laser with fixed cavity mirrors ($\xi = 0$) and the corresponding steady-state photon number is given by $N_{\rm photon,ss}^{\rm (convl)} \equiv N_{\rm photon,ss}|_{\delta_{\rm ss}=0}$. Without losing the generality, in what follows, we choose $\delta_0 = 2\pi \times 40$ MHz, leading to $\delta_{\rm ZPF} = -2\pi \times 14.1$ MHz. Such large $\delta_{\rm ZPF}$ is accessible in an experiment by reducing the cavity length and the effective mass of the mechanical oscillator[53]. It should be also noted that even reducing $\delta_0$ (or $\delta_{\rm ZPF}$) by a factor of 10 does not affect the main conclusions derived in this work.

Due to the nonzero $\delta_{\rm ss}$, $N_{\rm photon,ss}$ lacks the symmetry between red-detuned $\Delta < 0$ and blue-detuned $\Delta > 0$ regimes (Fig. 1b). The maximum of $N_{\rm photon,ss}$ occurs in the blue-detuned regime. Unlike the conventional lasers whose steady-state solutions are always stable, the steady-state solution of the optomechanical laser may be unstable to a small perturbation. One may perform the linear stability analysis to examine the stability of the steady-state solution in the lasing phase with $N_{\rm photon,ss} > 0$ (Supplementary Note 2). At an unstable steady state, $\langle \delta(t) \rangle$ undergoes a nearly harmonic oscillation around a nonzero average value (Fig. 1c). Whenever $\langle \delta(t) \rangle$ passes across zero, $\langle N_{\rm photon}(t) \rangle$ increases abruptly and then descends to zero in an oscillatory manner

because the cavity loss rate $\kappa$ greatly exceeds the damping rate $\Gamma$ of the mechanical oscillation. Figure 1d and e shows the photon number $N_{\mathrm{photon,ss}}$ in the $R - \Delta$ plane for different $Q$ factors. There exist several unstable zones, whose areas depend closely on the cavity $Q$ factor, in the lasing phase (Supplementary Movie 1). A large $Q$ increases the intracavity photon number and thus boosts the radiation pressure force. The resulting enhanced mechanical oscillation strongly affects the laser dynamics in return. Consequently, a steady-state that is stable for a low $Q$ may become unstable for a high $Q$ and the unstable zones are expanded. We consider the difference $\Delta N_{\mathrm{photon,ss}} \equiv N_{\mathrm{photon,ss}} - N_{\mathrm{photon,ss}}^{(\mathrm{convl})}$ between the steady-state photon numbers of the optomechanical laser $N_{\mathrm{photon,ss}}$ and the corresponding conventional laser $N_{\mathrm{photon,ss}}^{(\mathrm{convl})}$ with fixed mirrors ($\xi = 0$). As illustrated in Fig. 1f, g, $\Delta N_{\mathrm{photon,ss}}$ is mainly positive (negative) in the red-detuned $\Delta < 0$ (blue-detuned $\Delta > 0$) regime, indicating that the optomechanical coupling facilitates (supresses) the lasing action. It is also found that the ratio of $\Delta N_{\mathrm{photon,ss}}$ to $N_{\mathrm{photon,ss}}^{(\mathrm{convl})}$ is less than 1 percent for a low-$Q$ cavity and thus, the influence of the mechanical oscillation on the lasing dynamics may be viewed as a perturbation. In contrast, $\Delta N_{\mathrm{photon,ss}}/N_{\mathrm{photon,ss}}^{(\mathrm{convl})}$ can be over 20% for a high-$Q$ cavity due to the strong optomechanical coupling, and the mechanical oscillation cannot be treated as a perturbation to the lasing dynamics.

Besides the stability of steady-state solutions, the effects of the optomechanical coupling can be also revealed by the power spectral density $S_{\mathrm{photon}}(\omega)$ of the laser light. According to the Wiener–Khinchin theorem, when the system undergoes a stationary random process, one has $S_{\mathrm{photon}}(\omega) \propto \langle |\mathbb{F}[a(t)]|^2 \rangle$ with the Fourier transform $\mathbb{F}[a(t)] \equiv \int_{-\infty}^{+\infty} a(t)e^{-i\omega t}dt$ and the normalization $N_{\mathrm{photon,ss}} = \int_{-\infty}^{+\infty} S_{\mathrm{photon}}(\omega)d\omega$. For the conventional laser with fixed mirrors, the fluctuations of the macroscopic polarization of active atoms primarily contribute to the spectral broadening of the laser light[59]. For the optomechanical laser, the mechanical oscillation of the movable mirror may strongly affect $S_{\mathrm{photon}}(\omega)$. We numerically simulated the amplitude $a(t)$ of the intracavity field (see Methods) and computed $S_{\mathrm{photon}}(\omega)$ accordingly. As shown in the panel of $Q = 10^5$ in Fig. 2a, for a low-$Q$ cavity, $S_{\mathrm{photon}}(\omega)$ consists of the main peak surrounded by equally separated sidebands. Indeed, these sideband spikes directly result from the mechanical oscillator modulating the laser dynamics and the separation between two adjacent sidebands approximates $\Omega$. The main spectral peak is characterized by the central oscillation frequency $\omega_{\mathrm{L}}$ of the laser light and a full width at half maximum $\Delta\omega_{\mathrm{L}}$. The cavity pulling effect[60] shifts $\omega_{\mathrm{L}}$ away from the atomic transition frequency $\omega_{\mathrm{A}}$. However, unlike conventional laser whose central frequency $\omega_{\mathrm{L}}$ is independent of the photon number $N_{\mathrm{photon,ss}}$, the frequency difference $|\omega_{\mathrm{L}} - \omega_{\mathrm{A}}|$ of the optomechanical laser goes up linearly as $N_{\mathrm{photon,ss}}$ is enhanced because of the extra mechanical-displacement-induced detuning $\delta_{\mathrm{ss}}$. In the low-$Q$ limit, the perturbation approximation leads to

$$\omega_{\mathrm{L}} - \omega_{\mathrm{A}} \approx \frac{\Delta + \delta_{\mathrm{ss}}}{1 + \kappa/2\gamma_{\mathrm{eg}}}, \qquad (3)$$

whose validity can be confirmed by the panel of $Q = 10^5$ in Fig. 2b. The above equation allows one to evaluate $\delta_{\mathrm{ss}}$ (or the steady-state mechanical displacement $x_{\mathrm{ss}}$) by measuring the laser frequency $\omega_{\mathrm{L}}$. The sensitivity is given by $\partial x_{\mathrm{ss}}/\partial\omega_{\mathrm{L}} = \xi^{-1}(1 + \kappa/2\gamma_{\mathrm{eg}})$, which, interestingly, can be enhanced by increasing the cavity loss rate $\kappa$.

The spectral broadening $\Delta\omega_{\mathrm{L}}$ of the laser light may be predicted by using the Schawlow–Townes formula[61]

$$\Delta\omega_{\mathrm{L}} = \frac{\hbar\omega_{\mathrm{L}}}{2}\frac{\kappa^2}{P_{\mathrm{out}}}\frac{N_{\mathrm{e,ss}}}{N_{\mathrm{e,ss}} - N_{\mathrm{g,ss}}}\left[1 + \left(\frac{\Delta + \delta_{\mathrm{ss}}}{\gamma_{\mathrm{eg}} + \kappa/2}\right)^2\right]\left(\frac{\gamma_{\mathrm{eg}}}{\gamma_{\mathrm{eg}} + \kappa/2}\right)^2, \qquad (4)$$

with the laser output power $P_{\mathrm{out}}/\hbar\omega_{\mathrm{L}} = \kappa N_{\mathrm{photon,ss}}$ and the steady-state population $N_{\mathrm{u,ss}}$ of atoms in the $|u = e, g\rangle$ state. The panel of $Q = 10^5$ in Fig. 2b confirms the match between Eq. (4) and numerical results. When $|\Delta| \gg |\delta_{\mathrm{ss}}|$, increasing $R$ (or $N_{\mathrm{photon,ss}}$) reduces $\Delta\omega_L$. We also computed the power spectral density of the mechanical-displacement-induced detuning, $S_{\delta}(\omega) = \langle |\mathbb{F}[\delta(t)]|^2 \rangle$. Actually, $S_{\delta}(\omega)/\xi^2$ corresponds to the spectral density of the mechanical displacement $x(t)$. For a low $Q$, the spectrum $S_{\delta}(\omega)$ is single peaked at $\Omega$ (the panel of $Q = 10^5$ in Fig. 2c).

As the cavity $Q$ factor is increased, the main spectral peak in $S_{\mathrm{photon}}(\omega)$ is strongly broadened, i.e. $\Delta\omega_{\mathrm{L}}$ exceeds $\Omega$, and consequently the optomechanical-coupling-induced sidebands vanish (the panel of $Q = 10^6$ in Fig. 2a). This is attributed to the fact that a high $Q$ boosts the intracavity field and the resulting enhanced optomechanical-coupling maps more thermal fluctuations of the mechanical oscillator onto the lasing dynamics, thereby broadening the laser spectrum. Both Eqs. (3) and (4) fail in estimating $\omega_{\mathrm{L}}$ and $\Delta\omega_{\mathrm{L}}$ since the perturbation approximation becomes invalid (the panel of $Q = 10^6$ in Fig. 2b). Deriving the analytical expressions for $\omega_{\mathrm{L}}$ and $\Delta\omega_{\mathrm{L}}$ is impractical. The mechanical spectrum $S_{\delta}(\omega)$ also becomes broadened and, interestingly, the sideband peaks emerge at $\omega = m\Omega$ with $m \in \mathbb{Z}$ (the panel of $Q = 10^6$ in Fig. 2c). For a high enough $Q$, the spectrum $S_{\mathrm{photon}}(\omega)$ apparently violates the Lorentzian line shape as shown in the panel of $Q = 10^7$ in Fig. 2a. It is seen that $S_{\mathrm{photon}}(\omega)$ consists of a narrow high peak, corresponding to the lasing dynamics, and a wide background that arises from the thermal mechanical fluctuations. The linewidth $\Delta\omega_{\mathrm{L}}$ grows as $R$ is increased (the panel of $Q = 10^7$ in Fig. 2b). The sideband peaks in the mechanical spectrum $S_{\delta}(\omega)$ become more distinct (the panel of $Q = 10^7$ in Fig. 2c).

We are interested in the efficiency of the optical energy transfer to the spring–mass oscillator. Let us assume that the positions of both cavity mirrors are initially fixed, i.e. $x(t = 0) = 0$ and none energy is stored in the spring–mass oscillator, and the intracavity field reaches the steady state at a certain pump rate $R$ (Fig. 3a). Then, we let the mechanical oscillator (i.e. the movable mirror) free to move. Under the radiation pressure $F_{\mathrm{rad}}(t)$, the mechanical displacement $x(t)$ goes towards the steady-state value $x_{\mathrm{ss}}$. The work done by $F_{\mathrm{rad}}(t)$ during this process is given by $W = \int_{t=0}^{t=\infty} F_{\mathrm{rad}}(t)dx(t)$, which relies on the specific route of the movable mirror moving from $x(t = 0) = 0$ to $x(t = \infty) = x_{\mathrm{ss}}$. A portion of $W$ is dissipated through the damping of the spring–mass oscillator while the rest is converted to the elastic potential energy $U = m_{\mathrm{eff}}\Omega^2 x_{\mathrm{ss}}^2/2 = \hbar\delta_{\mathrm{ss}}^2/2\delta_0$ of the spring. One may define the efficiency of the optomechanical coupling as $\eta = U/W$. Figure 3b illustrates the dependence of $\eta$ on the pump rate $R$ for different cavity $Q$ factors. It is seen that $\eta$ grows strongly in the low-$R$ regime (still above the threshold) and then gradually declines after reaching a maximum that is close to unity. The efficiency $\eta$ is eventually saturated in the high-$R$ regime, denoting $W$ scales as $x_{\mathrm{ss}}^2$ for a large $R$. The saturation value of $\eta$ is about 0.5 for a low $Q$ while it approximates unity for a high $Q$.

Let us further examine the influence of optomechanical coupling on laser frequency stability. We assume that in addition to the radiation pressure $F_{\mathrm{rad}}(t)$ an extra environmental
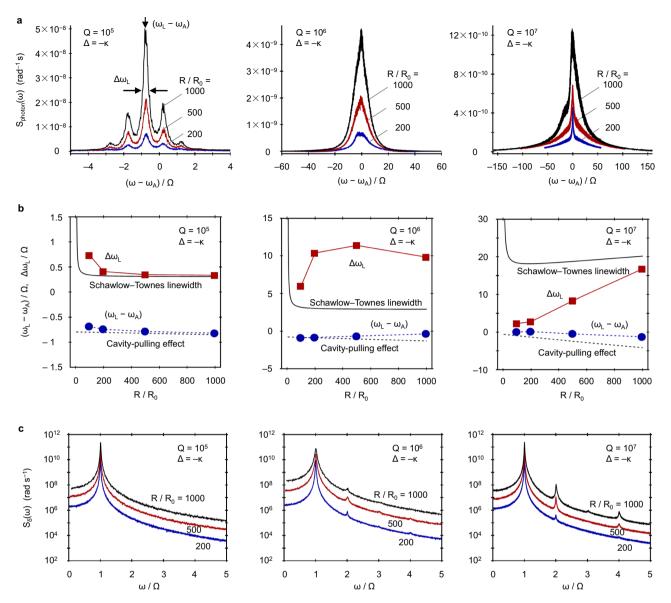
**Fig. 2 Power spectral densities of laser field and mechanical oscillation. a** Numerically simulated spectrum $S_{\text{photon}}(\omega)$ of the intracavity light field for different cavity $Q$ factors and pump rates $R$. The atom–cavity detuning is set at $\Delta = -\kappa$ with the cavity loss rate $\kappa$, and $R_0$ denotes the minimum pump threshold. At $\Delta = -\kappa$, the optomechanical laser has stable steady-state solutions for different $Q$ and $R$. The laser frequency $\omega_L$ is shifted from the atomic transition frequency $\omega_A$ and the laser linewidth (i.e. full width half maximum) is $\Delta\omega_L$. The mechanical oscillation frequency $\Omega$ is chosen as the frequency unit. **b** Dependence of laser frequency shift ($\omega_L - \omega_A$) and linewidth $\Delta\omega_L$ on the pump rate $R$ for different $Q$ factors with $\Delta = -\kappa$. Symbols corresponds to the numerical results. The curves derived from the cavity pulling effect and Schawlow–Townes formula are also plotted for comparison. **c** Numerically simulated spectrum $S_\delta(\omega)$ of the mechanical-displacement-induced detuning $\delta(t)$ for different $Q$ and $R$ with $\Delta = -\kappa$.

noise force $F_{\text{xtra}}(t)$ that arises from, for example, the ground vibration is exerted on the mechanical oscillator. We focus on the dimensionless signal $y(t) = \omega_L(t)/\omega_A$ with the laser frequency $\omega_L(t)$ perturbed by the mechanical vibration. The power spectral density of laser frequency fluctuations is given by $S_y(\omega) = \langle|\mathbb{F}[y(t)]|^2\rangle$, which can be measured by means of standard optical techniques in experiments[27]. The stability of $y(t)$ is commonly quantified by the Allan deviation $\sigma_y(\tau)$ with a sampling time $\tau$. We numerically simulated the optomechanical laser dynamics and extracted $y(t)$ from the trajectories of the laser amplitude $a(t)$.

For a low cavity $Q$ factor, the spectrum $S_y(\omega)$ scales as $\omega^0$ (Fig. 4a), that is, the white frequency noise plays the predominant role, and the corresponding Allan deviation follows the scaling law $\sigma_y(\tau) \propto 1/\sqrt{\tau}$ (Fig. 4b). When $F_{\text{xtra}}(t) = 0$, the atom–cavity

interface induces a wide peak located at $\omega = 2\mu$ in $S_y(\omega)$ and the optomechanical coupling gives rise to the other narrow peak at $\omega = \Omega$ (Fig. 4a). In comparison, we also computed the spectral density of frequency fluctuations of the corresponding conventional laser with fixed cavity mirrors ($\xi = 0$). Due to the weak optomechanical coupling in the low-$Q$ limit, optomechanical and conventional lasers have a similar spectral density of frequency fluctuations, except the spectral peak at $\omega = \Omega$ (Fig. 4a). As a result, their Allan deviations are close to each other, making it hardly to analyze mechanical fluctuations from the measurement of the laser frequency stability (Fig. 4b). Additionally, in the practical measurement the photon shot noise whose spectral density of frequency fluctuations is given by $(\kappa^2 + 4\Omega^2)/4\omega_A^2\kappa N_{\text{photon,ss}}$ sets the standard quantum limit to the photodetector's sensitivity[2]. As shown in Fig. 4a, only the spectral peaks at $\omega = \Omega$ and $\omega = 2\mu$ in $S_y(\omega)$
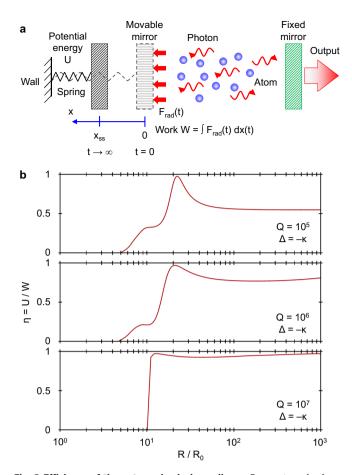
**a**



**b**



**Fig. 3 Efficiency of the optomechanical coupling. a** Energy transfer from the laser light to the spring–mass oscillator. Initially, the positions of two mirrors of the optical cavity are fixed and the intracavity field reaches the steady state. Then, the moveable mirror is free to move. The radiation pressure $F_{rad}(t)$ pushes the movable mirror away from the initial position $x(t = 0) = 0$. As the time goes infinity, $t \to \infty$, the position of the movable mirror approaches the steady-state displacement $x(t = \infty) = x_{ss}$. During this process, the radiation pressure does the work $W = \int_{t=0}^{t=\infty} F_{rad}(t)dx(t)$. When the moveable mirror is displaced at $x_{ss}$, the potential energy stored in the spring–mass oscillator is $U$. The energy conversion efficiency from $W$ to $U$ is given by $\eta = U/W$. **b** Efficiency $\eta$ vs. the pump rate $R$ for different cavity $Q$ factors. Here, $R_0$ is the minimum pump threshold. The atom–cavity detuning is set at $\Delta = -\kappa$ with the cavity loss rate $\kappa$.

exceed the shot-noise limit. The Allan deviation of the low-Q optomechanical laser is below the shot-noise-limited Allan deviation (Fig. 4b), impeding the detection of mechanical motion.

When $F_{xtra}(t) \neq 0$, the extra environmental noise source strongly elevates $S_y(\omega)$ above the shot noise (Fig. 4a). The spectral peak at $\omega = 2\mu$ in $S_y(\omega)$ disappears while the peak at $\omega = \Omega$ is retained. The Allan deviation $\sigma_y(\tau)$ with $F_{xtra}(t) \neq 0$ may exceed the shot-noise-limited $\sigma_y(\tau)$, providing a way to study the optomechanical coupling from the measurement of the laser frequency stability. Due to the frequency band-pass filtering feature of the mechanical oscillator, the noise force $F_{xtra}(t)$ in a certain color does not lead to the corresponding scaling of $\sigma_y(\tau)$ with respect to $\tau$. For instance, the pink-colored $F_{xtra}(t)$ with a power spectrum scaling as $\omega^{-1}$ may not lead to the scaling $\sigma_y(\tau) \propto \tau^0$ (Fig. 4b).

For a high cavity $Q$ factor, the enhanced intracavity field suppresses the shot noise and both $S_y(\omega)$ and $\sigma_y(\tau)$ with $F_{xtra}(t) = 0$

exceed the shot-noise limit (Fig. 4c, d), allowing for detecting the mechanical vibration. A spectral peak is presented at $\omega = \Omega$ in $S_y(\omega)$ of the optomechanical laser. The strong optomechanical coupling lifts the spectral density of frequency fluctuations of the optomechanical laser well above that of the corresponding conventional laser. That is, the laser frequency stability degrades since more mechanical fluctuations are mapped onto the lasing dynamics. This paves a way to evaluate the mechanical vibration from the measurement of the Allan deviation.

**One-atom active optomechanics.** In the above, we have discussed the active optomechanics in the macroscopic limit, where a large number of active atoms contribute to the intracavity field. We now consider the optomechanical microlaser with only one atom placed inside the optical cavity. Such a one-atom microlaser is feasible by means of current atom optical techniques[62–65]. The maximum pump rate $R$ is limited by half of the spontaneous emission rate of the atom from $(5p^{67}p)$ $^2P_{3/2}$ to $|e\rangle$, i.e. $R \sim 2\pi \times 0.35$ MHz. In the one-atom active optomechanics, the quantum nature of light plays the main role in the atom–cavity interaction since the intracavity field is significantly reduced. In addition, the quantum behaviour of the mechanical oscillator is highlighted at an extremely low temperature. Thus, the Heisenberg–Langevin method becomes invalid and the full quantum-mechanical treatment (based on the density matrix method) is necessarily employed. The complex field amplitude $a(t)$ is replaced with the photon annihilation operator $\hat{a}$ whose conjugate transpose gives the photon creation operator $\hat{a}^\dagger$. The harmonic mechanical oscillation is modelled as a vibrational mode with creation $\hat{b}^\dagger$ and annihilation $\hat{b}$ operators of phonons (see Methods). The coordinate operator takes the form $\hat{x} = x_{ZPF}(\hat{b} + \hat{b}^\dagger)$ and the optomechanical interaction is written as $\hbar\delta_{ZPF}\hat{a}^\dagger\hat{a}(\hat{b} + \hat{b}^\dagger)$ with the vacuum optomechanical-coupling strength $\delta_{ZPF} = \xi x_{ZPF}$. The dynamics of the microscopic system is governed by the master equation of the density matrix operator $\hat{\rho}(t)$ of the system (Supplementary Note 3). The photon and phonon numbers are given by $N_{photon}(t) = \text{Tr}[\hat{a}^\dagger\hat{a}\hat{\rho}(t)]$ and $N_{phonon}(t) = \text{Tr}[\hat{b}^\dagger\hat{b}\hat{\rho}(t)]$, respectively, with the trace operation $\text{Tr}(\dots)$. We set the cavity $Q$ factor at $10^7$ and the phonon frequency $\Omega$ is chosen as $2\pi \times 100$ MHz. That is, the optomechanical system accesses the sideband-resolved regime with $\kappa < \Omega$, highlighting the quantum features of the photon–phonon interface. We numerically study this one-atom optomechanical microlaser.

The dependences of the steady-state photon $N_{photon,ss}$ and phonon $N_{phonon,ss}$ numbers on the atom–cavity detuning $\Delta$ are shown in Fig. 5a and b, respectively. It is seen that $N_{photon,ss}$ differs much from that of the corresponding common one-atom microlaser with fixed mirrors (i.e. $\xi = 0$). Due to $\kappa < \Omega$, the transitions between the product states $|n_{photon}\rangle \otimes |e\rangle \otimes |n_{phonon}\rangle$ and $|n_{photon} + 1\rangle \otimes |g\rangle \otimes |n'_{phonon}\rangle$ are well resolved. Here, $|n_{photon}\rangle$ and $|n_{phonon}\rangle$ denote the Fock (number) states of photons and phonons, respectively. Consequently, several submaxima of $N_{photon,ss}$ are presented in the $N_{photon,ss} - \Delta$ curve and the separation between two adjacent submaxima approximates $\Omega$. For a large $\Delta$, $N_{phonon,ss}$ decreases strongly because of the weakened atom–cavity interaction. The $N_{phonon,ss} - \Delta$ curve also exhibits several submaxima/subminima. Comparing $N_{phonon,ss}$ with the average number $n_{thrm}$ of thermal quanta, one obtains the heating regime with $N_{phonon,ss} > n_{thrm}$ and the cooling regime with $N_{phonon,ss} < n_{thrm}$ (Fig. 5b). The boundary between two regimes is located on the blue-detuned side of the atomic transition. Tuning
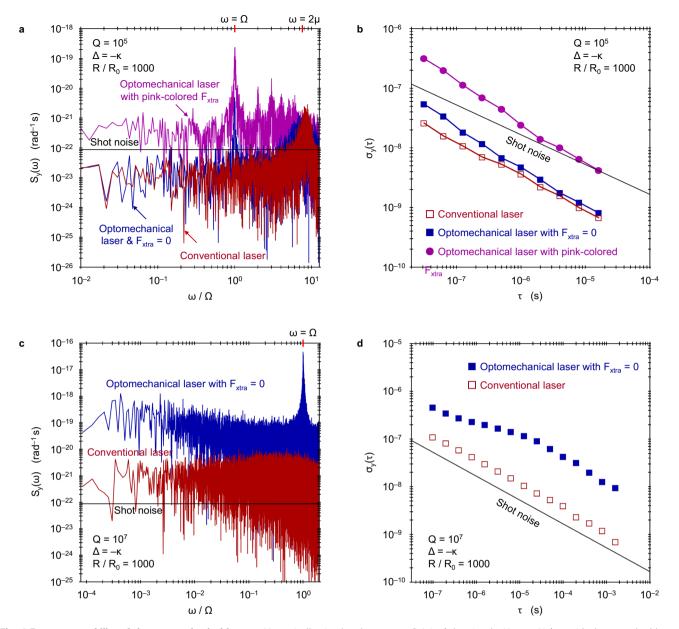
**Fig. 4 Frequency stability of the optomechanical laser. a** Numerically simulated spectrum $S_y(\omega)$ of the signal $y(t) = \omega_L(t)/\omega_A$ with the perturbed laser frequency $\omega_L(t)$ and the atomic transition frequency $\omega_A$. The optical cavity has a low $Q$ factor of $10^5$. For the optomechanical laser, the optical cavity has a movable mirror. For the corresponding conventional laser, the positions of both cavity mirrors are fixed. In addition to the photon radiation pressure, an extra environmental noise force $F_{xtra}(t)$ is exerted upon the mechanical oscillator whose oscillation frequency $\Omega$ is chosen as the frequency unit. The pink-colored noise force $F_{xtra}(t)$ is chosen as $F_{xtra}(t) = 200\hbar\xi \cdot F(t)$ with the frequency pull parameter $\xi$. The spectral density of the noise function $F(t)$ is given by $1/\omega$. The pump rate $R$ is set at $10^3 R_0$ with the minimum pump threshold $R_0$ and the atom–cavity detuning is chosen as $\Delta = -\kappa$ with the cavity loss rate $\kappa$. The spectra $S_y(\omega)$ under different conditions are plotted. Two spectral peaks are presented in $S_y(\omega)$ at around $\omega = 2\mu$ and $\omega = \Omega$ with the atom–cavity coupling strength $\mu$ and the mechanical oscillation frequency $\Omega$. The corresponding Allan deviations $\sigma_y(\tau)$ are shown in **b. c, d** Spectra $S_y(\omega)$ and Allan deviations $\sigma_y(\tau)$ with a high $Q$ factor of $10^7$ under different conditions. For comparison, the shot-noise-limited spectra and Allan deviations have been inserted.

$\Delta$ allows for exciting/suppressing the mechanical oscillation. Due to the huge difference between the lifetimes of photons and phonons, $\kappa \gg \Gamma$, the intracavity photons are mainly distributed in the vacuum state $|n_{photon} = 0\rangle$ while the phonons can be populated on the high number states (Fig. 5c). The phonon distribution, especially the probability in $|n_{phonon} = 0\rangle$, strongly depends on the detuning $\Delta$ (Supplementary Note 4).

We employ the second-order correlation function $g_{photon}^{(2)}(\tau) = \langle \hat{a}^\dagger(t)\hat{a}^\dagger(t+\tau)\hat{a}(t+\tau)\hat{a}(t)\rangle / \langle \hat{a}^\dagger(t)\hat{a}(t)\rangle^2$ at the zero-time delay

$\tau = 0$ to characterize the photon statistics. Here, $\hat{a}^\dagger(t)$ and $\hat{a}(t)$ are the photon operators in the Heisenberg picture. As shown in Fig. 5d, $g_{photon}^{(2)}(\tau = 0)$ is well below unity, indicating the antibunching of photon emission, and appears an oscillatory behaviour vs. the atom–cavity detuning $\Delta$ due to the well-resolved phonon states (i.e. $\kappa < \Omega$). In comparison to the common one-atom microlaser with fixed mirrors (i.e. $\xi = 0$), one finds that $g_{photon}^{(2)}(\tau = 0)$ is lower (higher) than that of the common one-atom microlaser in the red-detuned (blue-detuned) regime with $\Delta < 0$ ($\Delta > 0$). We also
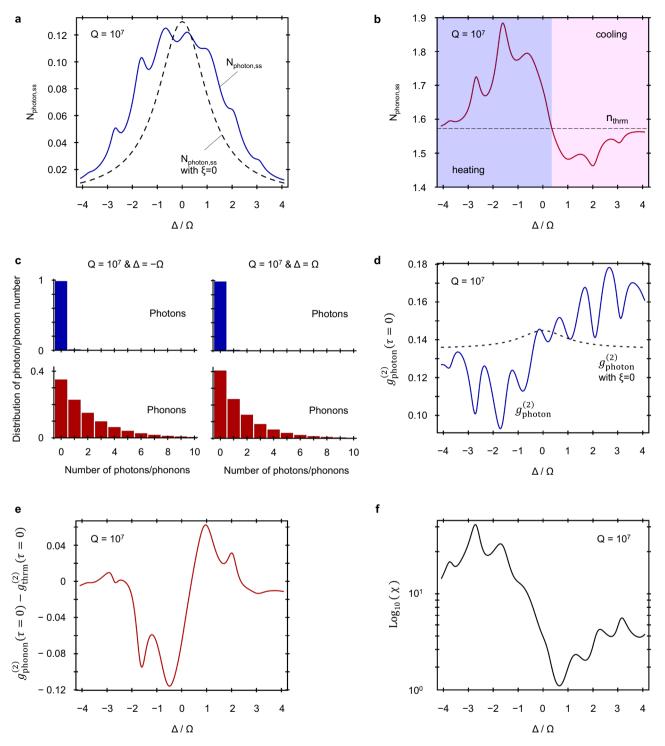
**Fig. 5 Steady-state solutions of one-atom optomechanical microlaser. a** Steady-state number $N_{\text{photon,ss}}$ of intracavity photons as a function of the atom–cavity detuning $\Delta$. For comparison, $N_{\text{photon,ss}}$ of the corresponding one-atom microlaser in the absence of the optomechanical coupling (i.e. zero optomechanical constant $\xi = 0$) is also plotted. The mechanical oscillation frequency $\Omega$ is chosen as the frequency unit. The corresponding steady-state number $N_{\text{phonon,ss}}$ of phonons is shown in **b**. The blue shade denotes the heating regime with $N_{\text{phonon,ss}} > n_{\text{thrm}}$ while the pink shade corresponds to the cooling regime with $N_{\text{phonon,ss}} < n_{\text{thrm}}$. Here, $n_{\text{thrm}}$ denotes the average number of thermal quanta. **c** Distributions of photon and phonon numbers with $\Delta = \pm\Omega$. **d** Dependence of the second-order correlation function $g^{(2)}_{\text{photon}}(\tau)$ of photons at the zero-time delay $\tau = 0$ on the detuning $\Delta$. The second-order correlation function of the common one-atom microlaser with fixed cavity mirrors ($\xi = 0$) is also plotted for comparison. **e** Second-order correlation function $g^{(2)}_{\text{phonon}}(\tau = 0)$ of phonons relative to the second-order correlation function $g^{(2)}_{\text{thrm}}(\tau = 0)$ of the thermal state. **f** Ratio $\chi \equiv [g^{(2)}_{\text{photon-phonon}}(0)]^2 / g^{(1)}_{\text{photon}}(0) g^{(1)}_{\text{phonon}}(0)$ vs. the atom–cavity detuning $\Delta$. Here, $g^{(2)}_{\text{photon-phonon}}(0)$ denotes the cross-correlation function between photons and phonons. For all curves, the cavity $Q$ factor is $10^7$ and the pump rate is set at $R \sim 2\pi \times 0.35$ MHz.

compute the second-order correlation function $g^{(2)}_{\text{phonon}}(\tau) = \langle \hat{b}^\dagger(t)\hat{b}^\dagger(t+\tau)\hat{b}(t+\tau)\hat{b}(t)\rangle / \langle \hat{b}^\dagger(t)\hat{b}(t)\rangle^2$ of phonons. It is found that unlike $g^{(2)}_{\text{photon}}(\tau = 0)$, $g^{(2)}_{\text{phonon}}(\tau = 0)$ is always above unity, i.e. the bunching of phonons. As illustrated in Fig. 5e, $g^{(2)}_{\text{phonon}}(\tau = 0)$ exhibits a dispersion behaviour around $\Delta = 0$. For an ensemble of thermal quanta, the corresponding second-order correlation function $g^{(2)}_{\text{thrm}}(\tau = 0)$ is equal to two[66]. The function $g^{(2)}_{\text{phonon}}(\tau = 0)$ is lower (higher) than $g^{(2)}_{\text{thrm}}(\tau = 0)$ mainly in the red-detuned (blue-detuned) regime with $\Delta < 0$ ($\Delta > 0$). We further examine the Cauchy–Schwarz inequality[67] $\chi \equiv [g^{(2)}_{\text{photon-phonon}}(0)]^2 / g^{(2)}_{\text{photon}}(0)g^{(2)}_{\text{phonon}}(0) < 1$ with the cross-correlation function $g^{(2)}_{\text{photon-phonon}}(\tau) = \langle \hat{a}^\dagger(t)\hat{b}^\dagger(t+\tau)\hat{b}(t+\tau)\hat{a}(t)\rangle / \langle \hat{a}^\dagger(t)\hat{a}(t)\rangle\langle \hat{b}^\dagger(t)\hat{b}(t)\rangle$ between photons and phonons. Figure 5f shows that $\chi$ is larger than unity within the detuning regime of interest. This violation of the Cauchy–Schwarz inequality is a concrete measure for the nonclassical photon–phonon pair generation[68,69]. The minimum of $\chi$ approaches unity and occurs at the heating–cooling boundary. Compared to nonclassical correlations for photon pairs[70], generating nonclassical correlations between single photons and phonons with six orders of magnitude difference in frequency is more challenging, and here we provide a potential way. The nonclassical photon–phonon pairs can be used to remotely control mechanical states and allow for mechanics-based long-distance quantum communication[71].

The first-order correlation functions of photons and phonons are defined as $g^{(1)}_{\text{photon}}(\tau) = \langle \hat{a}^\dagger(t)\hat{a}(t+\tau)\rangle / \langle \hat{a}^\dagger(t)\hat{a}(t)\rangle$ and $g^{(1)}_{\text{phonon}}(\tau) = \langle \hat{b}^\dagger(t)\hat{b}(t+\tau)\rangle / \langle \hat{b}^\dagger(t)\hat{b}(t)\rangle$, respectively. It is seen from Fig. 6a that $g^{(1)}_{\text{photon}}(\tau)$ rapidly decays from unity to zero while $g^{(1)}_{\text{phonon}}(\tau)$ experiences a long-term damped oscillation process. That is, the phonons possess a lifetime much longer than that of the photons. The Fourier transform of $g^{(1)}_{\text{photon}}(\tau)$ gives the spectrum of photons, $S_{\text{photon}}(\omega) \propto \mathbb{F}[g^{(1)}_{\text{photon}}(\tau)]$. We find that the spectrum of the one-atom optomechanical microlaser is more complex than that of the corresponding one-atom microlaser with fixed mirrors (Fig. 6b). Multiple peaks exhibit in $S_{\text{photon}}(\omega)$ of the one-atom optomechanical microlaser. Two central peaks result from the atom–cavity coupling while others are located at $\omega = \pm m\Omega$ with a non-negative integer $m$ and correspond to the photon–phonon interaction. The appearance of photon–phonon-interaction-induced spectral peaks is a direct consequence of the system operating in the resolved-sideband regime $\kappa < \Omega$. We also calculated the spectrum $S_{\text{phonon}}(\omega) \propto \mathbb{F}[g^{(1)}_{\text{phonon}}(\tau)]$ of phonons and found $S_{\text{phonon}}(\omega)$ is always single peaked (Fig. 6c). The linewidth and central frequency of $S_{\text{phonon}}(\omega)$ depends less on the atom–cavity detuning $\Delta$ (Fig. 6d), that is, $S_{\text{phonon}}(\omega)$ is mainly determined by the thermal fluctuations.

## Discussion

Besides the frequency shift and optical phase measurements that are usually employed in passive optomechanics, the mechanical motion may be also detected by measuring the laser intensity, spectral broadening, and laser frequency stability in the active optomechanics. Generally, the intracavity field in the typical passive optomechanics comes from an external driving beam and can be adjusted freely by changing the driving power and the detuning between the optical cavity and the driving beam. In contrast, the energy source in active optomechanics is the intra-cavity active medium. The lasing action occurs when the optical gain exceeds the optical loss. Thus, an active optomechanical system may act as a light source, whose output can be tuned by controlling the mechanical motion, in a photonic integrated circuit[30]. In addition, the passive optomechanical system may exhibit a bistable behaviour, i.e. two stable steady-state solutions and one unstable steady-state solution[2]. However, the active optomechanical system has at most one stable steady-state. This may be ascribed to the extra condition imposed by the lasing threshold. Moreover, in passive optomechanics, when the cavity is pumped in a detuned manner, the radiation pressure force exerted on the mechanical oscillator becomes viscous, i.e. dynamic backaction. This effect has been applied to suppress the mechanical motion of the optical cavity, i.e. optomechanical cooling[11]. However, the situation becomes more complicated in macroscopic active optomechanics. Since the intracavity field is completely determined by the active optomechanical system itself, it is challenging to fulfil the optomechanical-cooling condition[72] $N_{\text{photon,ss}}\Delta\omega_L \ll \kappa$. Furthermore, unlike the passive opto-mechanics, the active operation manner reveals the intrinsic properties (such as stability and temporal coherence) of the optomechanical systems.

Up to now, the active optomechanics has been only demon-strated on the vertical-cavity surface-emitting lasers[30–32]. Other laser platforms that are potentially utilized to implement the active optomechanics include Fabry–Pérot resonators with neutral atom gases[36,73], whispering-gallery-mode microcavities[74–76]/droplets[77,78] doped with ions and mole-cules, and fibre microcavities[79,80]. The one-atom microlaser has been demonstrated based on the schemes of an atom/ion trap-ped in a high-finesse optical cavity[62,63], a quantum dot embedded in a nanocavity[64], and a nitrogen-vacancy centre in diamond[65]. The optomechanical coupling may be induced by inserting a nanorod/nanowire into the optical cavity[53] or bringing a silicon nitride nanomechanical string close to a sili-con microdisk/microtoroid[81,82]. These nano-scaled objects have an effective mass as small as a few pictograms or even a few femtograms[54] and a mechanical oscillation frequency of the order of megahertz. The single-photon optomechanical-cou-pling strength can reach $\sim 2\pi \times 1$ MHz. Another possible plat-form is soap bubbles[83], which may be further extended to optomechanical single-molecule detection[19]. Although here we only discussed the coupling between one optical cavity mode and one mechanical mode, the analysis can be extended to the active optomechanics with multiple mechanical modes[27]. The inter-mechanical-mode coupling mediated by light may lead to nonlinear phenomena.

In order to suppress the influence of thermal fluctuations on the active optomechanical dynamics, the average number $n_{\text{thrm}}$ of thermal quanta should be sufficiently reduced by means of, for examples, raising the mechanical oscillation frequency and operating at cryogenic temperature. An integrated optical and nanomechanical resonator formed on a microchip can have a mechanical oscillation frequency $\Omega$ of a few gigahertzs[15]. Despite the difficulty, a cryogenic temperature below 10 mK is feasible[84,85]. When $\Omega \sim 2\pi \times 1$ GHz, $n_{\text{thrm}}$ is much less than unity[68], highlighting the quantum nature of phonons and enabling quantum control of single phonons through single optical photons. Besides optical modes, mechanical oscillators also coherently interact with other physical quantum systems, such as spins[86] and superconducting circuits[87], allowing for the mechanics-based quantum information transfer and remote quantum state control.
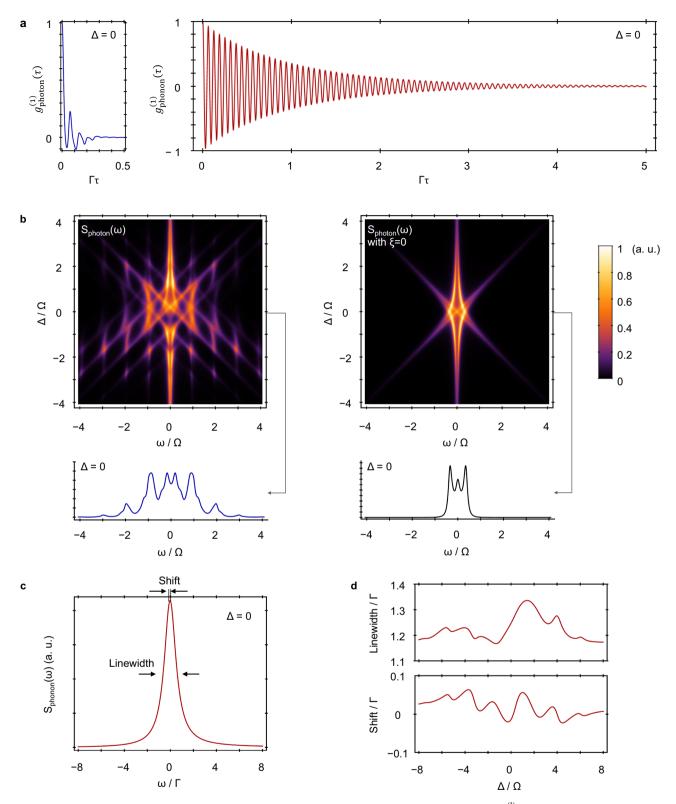
**Fig. 6 Photon and phonon spectra of one-atom optomechanical microlaser. a** First-order correlation functions $g^{(1)}_{\text{photon}}(\tau)$ of intracavity photons and $g^{(1)}_{\text{phonon}}(\tau)$ of phonons with the atom–cavity detuning $\Delta = 0$. Here, $\tau$ denotes with the time delay and $\Gamma$ is the decay rate of phonons. **b** Dependence of the power spectral density $S_{\text{photon}}(\omega)$ of photons on $\Delta$. The mechanical oscillation frequency $\Omega$ is chosen as the frequency unit. By comparison, the spectrum of the common one-atom microlaser with zero optomechanical constant $\xi = 0$ is also plotted. **c** Spectrum $S_{\text{phonon}}(\omega)$ of phonons with $\Delta = 0$. **d** Dependence of the linewidth and shift of $S_{\text{phonon}}(\omega)$ on $\Delta$. Linewidth and shift are in units of the damping rate $\Gamma$ of the mechanical oscillator. For all curves, the cavity $Q$ factor is $10^7$ and the pump rate is set at $R \sim 2\pi \times 0.35$ MHz.

## Methods

**Classical optomechanical system**. The dynamics of a macroscopic laser system is governed by a set of c-number Heisenberg–Langevin equations[69]

$$\dot{N}_e(t) = R - \gamma'_e N_e(t) - i\mu[M^*(t)a(t) - a^*(t)M(t)], \tag{5a}$$

$$\dot{N}_g(t) = -\gamma_g N_g(t) + \gamma_e N_e(t) + i\mu[M^*(t)a(t) - a^*(t)M(t)], \tag{5b}$$

$$\dot{M}(t) = -\gamma_{eg}M(t) + i\mu[N_e(t) - N_g(t)]a(t) + F_M(t), \tag{5c}$$

$$\dot{a}(t) = [-\kappa/2 - i\Delta - i\delta(t)]a(t) - i\mu M(t) + F_a(t). \tag{5d}$$

Here, $N_{u=e,g}(t)$ denotes the population of atoms in the $|u = e, g\rangle$ state, $M(t)$ accounts for the macroscopic polarization of atoms, and $\delta(t)$ corresponds to the mechanical-displacement-induced detuning. In above equations, we have only included the Langevin force $F_M(t)$ associated with $M(t)$ and omitted the Langevin forces acting on $N_{u=e,g}(t)$ since the laser spectral broadening arises predominantly from the fluctuations in $M(t)$. The noise $F_M(t)$ has the correlation functions $\langle F_M(t)\rangle = 0$, $\langle F_M(t)F_M(t')\rangle = 2i\mu\langle M(t)a(t)\rangle\delta(t-t')$, and $\langle F^*_M(t)F_M(t')\rangle = [(2\gamma_{eg} - \gamma'_e)\langle N_e(t)\rangle + R]\delta(t-t')$. Further, the Langevin force $F_a(t)$ acting on the optical cavity is negligible under the assumption of low temperature $T$.

The mechanical displacement $x(t)$ is driven by the radiation pressure force $F_{rad}(t) = -\hbar\xi N_{photon}(t)$ with the intracavity photon number $N_{photon}(t) = |a(t)|^2$. The equation of motion of the mechanical-displacement-induced detuning $\delta(t) = \xi x(t)$ is given by

$$\ddot{\delta}(t) + \Gamma\dot{\delta}(t) + \Omega^2\delta(t) = \xi[F_{rad}(t) + F_{thrm}(t) + F_{xtra}(t)]/m_{eff}. \tag{6}$$

In above equation, the thermal force noise $F_{thrm}(t) = (\hbar\sqrt{\Gamma}/x_{ZPF})f_{thrm}(t)$ acting on the movable mirror has been included. The white noise $f_{thrm}(t)$ has the correlation functions $\langle f_{thrm}(t)\rangle = 0$ and $\langle f_{thrm}(t)f_{thrm}(t')\rangle = n_{thrm}\delta(t-t')$ with the average number $n_{thrm}$ of thermal quanta. The extra environmental force $F_{xtra}(t)$ is introduced to include all other noise sources such as ground vibrations. For the macroscopic optomechanics, we choose the frequency $\Omega = 2\pi\times 10$ MHz and $Q_m = 10^2$ of the mechanical oscillator and the environmental temperature $T = 1$ K with $n_{thrm} \approx 2083$. The active optomechanics can be investigated by self-consistently solving Eqs. (5) and (6).

Setting $\dot{N}_{u=e,g}(t) = \dot{M}(t) = \dot{a}(t) = \ddot{\delta}(t) = \dot{\delta}(t) = 0$ and dropping all Langevin noises, one obtains the steady-state solutions $N_{photon,ss} \equiv \langle N_{photon}(t\to\infty)\rangle$ and $\delta_{ss} \equiv \langle\delta(t\to\infty)\rangle$ from Eqs. (5) and (6). The stability of the derived steady-state solutions can be examined by performing the linear analysis. We write each variable as a sum of its steady-state value and a small fluctuation, e.g. $N_e(t) = N_{e,ss} + \epsilon_{N_e}(t)$. Then, Eqs. (5) and (6) are reduced to a matrix linear differential equation $\dot{\epsilon} = \mathbf{L}\epsilon$ with $\epsilon = (\epsilon_{N_e}\dots\epsilon_\delta)^T$ (Supplementary Note 2). A stable steady-state solution requires that the real parts of all eigenvalues of the $7\times 7$ matrix $\mathbf{L}$ are all negative.

**One-atom optomechanical microlaser**. The active optomechanical system with only one atom placed inside the optical cavity can be described by the Hamiltonian

$$\hat{H}/\hbar = \omega_C\hat{a}^\dagger\hat{a} + \frac{\omega_A}{2}(\hat{\sigma}_{ee} - \hat{\sigma}_{gg}) + \Omega\hat{b}^\dagger\hat{b} + \mu(\hat{\sigma}_{eg}\hat{a} + \hat{a}^\dagger\hat{\sigma}_{ge}) + \delta_{ZPF}\hat{a}^\dagger\hat{a}(\hat{b} + \hat{b}^\dagger), \tag{7}$$

with the photon creation $(\hat{a}^\dagger)$ and annihilation $(\hat{a})$ operators and the phonon creation $(\hat{b}^\dagger)$ and annihilation $(\hat{b})$ operators of the quantum-mechanical oscillator. The population operators of the atom are given by $\hat{\sigma}_{ee} = |e\rangle\langle e|$ and $\hat{\sigma}_{gg} = |g\rangle\langle g|$. The atomic lowering operator is defined as $\hat{\sigma}_{ge} = |g\rangle\langle e|$ and the raising operator takes the form $\hat{\sigma}_{eg} = |e\rangle\langle g|$. The first three terms in $\hat{H}$ denote the free energies of photons, atom, and phonons, respectively. The fourth term in $\hat{H}$ corresponds to the atom–cavity interaction while the last them in $\hat{H}$ gives the optomechanical coupling between photons and phonons. The Hilbert space is spanned by $\{|n_{photon}\rangle \otimes |u\rangle \otimes |n_{phonon}\rangle; n_{photon}, n_{phonon} \in \mathbb{Z}_0^+; u = e, g, s\}$ with the photon number state $|n_{photon}\rangle$, the atomic state $|u\rangle$, and the phonon number state $|n_{phonon}\rangle$. Here, an extra atomic state $|s\rangle$ is introduced to model the pumping process of the atom[88]. The symbol $\mathbb{Z}_0^+$ denotes the non-negative integers. The dynamics of the one-atom optomechanical system follows the Lindblad master equation[89]

$$\frac{d}{dt}\hat{\rho} = -i[\hat{H}/\hbar, \hat{\rho}] + \frac{\kappa}{2}D[\hat{a}]\hat{\rho} + \frac{\Gamma}{2}(n_{thrm}+1)D[\hat{b}]\hat{\rho} + \frac{\Gamma}{2}n_{thrm}D[\hat{b}^\dagger]\hat{\rho}$$
$$+ \frac{R}{2}D[\hat{\sigma}_{se}]\hat{\rho} + \frac{(\gamma'_e-\gamma_e)}{2}D[\hat{\sigma}_{es}]\hat{\rho} + \frac{\gamma_e}{2}D[\hat{\sigma}_{eg}]\hat{\rho} + \frac{\gamma_g}{2}D[\hat{\sigma}_{gs}]\hat{\rho}, \tag{8}$$

where $\hat{\rho}$ is the system's density operator and the dissipative term, for example, $D[\hat{a}]\hat{\rho} = 2\hat{a}\hat{\rho}\hat{a}^\dagger - \hat{a}^\dagger\hat{a}\hat{\rho} - \hat{\rho}\hat{a}^\dagger\hat{a}$ denotes the photons escaping from the optical cavity. The photon and phonon numbers are given by $N_{photon}(t) = \langle\hat{a}^\dagger(t)\hat{a}(t)\rangle = \mathrm{Tr}[\hat{a}^\dagger\hat{a}\hat{\rho}(t)]$ and $N_{phonon}(t) = \langle\hat{b}^\dagger(t)\hat{b}(t)\rangle = \mathrm{Tr}[\hat{b}^\dagger\hat{b}\hat{\rho}(t)]$, respectively. When the pump laser is strong enough, the pump rate $R$ approximates the half of the decay

rate of the atom from $(5p^67p)\ ^2P_{3/2}$ to $|e\rangle$, i.e. $R \sim 2\pi\times 0.35$ MHz. For the microscopic optomechanics, in order to carry out the numerical simulation we choose the mechanical frequency $\Omega = 2\pi\times 100$ MHz and $Q_m = 10^2$ of the mechanical oscillator and the environmental temperature[56,57] $T = 10$ mK with the average number $n_{thrm} \approx 1.6$ of thermal quanta. The master Eq. (8) may be solved by using the diagonalization method[89]. The two-time correlation function $\langle\hat{A}(t)\hat{B}(t+\tau)\rangle$ between two arbitrary operators $\hat{A}$ and $\hat{B}$ can be calculated by using the quantum regression theorem[66].

## References

1. Schliesser, A. & Kippenberg, T. J. In *Advances in Atomic, Molecular, and Optical Physics* Vol. 58 (eds. P. Berman, Arimondo, E. & Lin, C.) Ch. 5, 207–323 (Academic, 2010).
2. Aspelmeyer, M., Kippenberg, T. J. & Marquardt, F. Cavity optomechanics. *Rev. Mod. Phys.* **86**, 1391–1452 (2014).
3. Kippenberg, T. J. & Vahala, K. J. Cavity opto-mechanics. *Opt. Express* **15**, 17172–17205 (2007).
4. Corbitt, T. et al. An all-optical trap for a gram-scale mirror. *Phys. Rev. Lett.* **98**, 150802 (2007).
5. Corbitt, T. et al. Optical dilution and feedback cooling of a gram-scale oscillator to 6.9 mK. *Phys. Rev. Lett.* **99**, 160801 (2007).
6. Arcizet, O., Cohadon, P.-F., Briant, T., Pinard, M. & Heidmann, A. Radiation-pressure cooling and optomechanical instability of a micromirror. *Nature* **444**, 71–74 (2006).
7. Anguiano, S. et al. Micropillar resonators for optomechanics in the extremely high 19–95-GHz frequency range. *Phys. Rev. Lett.* **118**, 263901 (2017).
8. Thompson, J. et al. Strong dispersive coupling of a high-finesse cavity to a micromechanical membrane. *Nature* **452**, 72–75 (2008).
9. Verhagen, E., Deléglise, S., Weis, S., Schliesser, A. & Kippenberg, T. J. Quantum-coherent coupling of a mechanical oscillator to an optical cavity mode. *Nature* **482**, 63–67 (2012).
10. Schliesser, A., Riviere, R., Anetsberger, G., Arcizet, O. & Kippenberg, T. Resolved-sideband cooling of a micromechanical oscillator. *Nat. Phys.* **4**, 415–419 (2008).
11. Schliesser, A., Del'Haye, P., Nooshi, N., Vahala, K. J. & Kippenberg, T. J. Radiation pressure cooling of a micromechanical oscillator using dynamical backaction. *Phys. Rev. Lett.* **97**, 243905 (2006).
12. Yu, D. et al. Whispering-gallery-mode sensors for biological and physical sensing. *Nat. Rev. Methods Prim.* **1**, 83 (2021).
13. Favero, I. et al. Fluctuating nanomechanical system in a high finesse optical microcavity. *Opt. Express* **17**, 12813–412820 (2009).
14. Kippenberg, T. J., Rokhsari, H., Carmon, T., Scherer, A. & Vahala, K. J. Analysis of radiation-pressure induced mechanical oscillation of an optical microcavity. *Phys. Rev. Lett.* **95**, 033901 (2005).
15. Chan, J. et al. Laser cooling of a nanomechanical oscillator into its quantum ground state. *Nature* **478**, 89–92 (2011).
16. Srinivasan, K., Miao, H., Rakher, M. T., Davanço, M. & Aksyuk, V. Optomechanical transduction of an integrated silicon cantilever probe using a microdisk resonator. *Nano Lett.* **11**, 791–797 (2011).
17. Arcizet, O. et al. High-sensitivity optical monitoring of a micromechanical resonator with a quantum-limited optomechanical sensor. *Phys. Rev. Lett.* **97**, 133601 (2006).
18. Eichenfield, M. et al. A picogram- and nanometre-scale photonic-crystal optomechanical cavity. *Nature* **459**, 550–555 (2009).
19. Yu, W., Jiang, W. C., Lin, Q. & Lu, T. Cavity optomechanical spring sensing of single molecules. *Nat. Commun.* **7**, 12311 (2016).
20. Yang, C., Wei, X., Sheng, J. & Wu, H. Phonon heat transport in cavity-mediated optomechanical nanoresonators. *Nat. Commun.* **11**, 4656 (2020).
21. Labeyrie, G. et al. Optomechanical self-structuring in a cold atomic gas. *Nat. Photon* **8**, 321–325 (2014).
22. Jöckel, A. et al. Sympathetic cooling of a membrane oscillator in a hybrid mechanical–atomic system. *Nat. Nanotech.* **10**, 55–59 (2015).

23. Vitali, D. et al. Optomechanical entanglement between a movable mirror and a cavity field. *Phys. Rev. Lett.* **98**, 030405 (2007).

24. Yuen, H. P. & Chan, V. W. S. Noise in homodyne and heterodyne detection. *Opt. Lett.* **8**, 177–179 (1983).

25. Hansch, T. W. & Couillaud, B. Laser frequency stabilization by polarization spectroscopy of a reflecting reference cavity. *Opt. Commun.* **35**, 441–444 (1980).

26. Drever, R. W. P. et al. Laser phase and frequency stabilization using an optical resonator. *Appl. Phys. B* **31**, 97–105 (1983).

27. Schliesser, A., Anetsberger, G., Rivière, R., Arcizet, O. & Kippenberg, T. J. High-sensitivity monitoring of micromechanical vibration using optical whispering gallery mode resonators. *N. J. Phys.* **10**, 095015 (2008).

28. Ge, L., Faez, S., Marquardt, F. & Türeci, H. E. Gain-tunable optomechanical cooling in a laser cavity. *Phys. Rev. A* **87**, 053839 (2013).

29. Wisniewski, H., Richardson, L., Hines, A., Laurain, A. & Guzmán, F. Optomechanical lasers for inertial sensing. *J. Opt. Soc. Am. A* **37**, B87–B92 (2020).

30. Huang, M. C. Y., Zhou, Y. & Chang-Hasnain, C. J. A nanoelectromechanical tunable laser. *Nat. Photon* **2**, 180–184 (2008).

31. Yang, W. et al. Laser optomechanics. *Sci. Rep.* **5**, 13700 (2015).

32. Czerniuk, T. et al. Lasing from active optomechanical resonators. *Nat. Commun.* **5**, 4038 (2014).

33. Yu, D. & Vollmer, F. Microscale whispering-gallery-mode light sources with lattice-confined atoms. *Sci. Rep.* **11**, 13899 (2021).

34. Gorodetsky, M. L., Schliesser, A., Anetsberger, G., Deleglise, S. & Kippenberg, T. J. Determination of the vacuum optomechanical coupling rate using frequency noise calibration. *Opt. Express* **18**, 23236–23246 (2010).

35. Shi, T., Pan, D., Chang, P., Shang, H. & Chen, J. A highly integrated single-mode 1064 nm laser with 8.5 kHz linewidth for dual-wavelength active optical clock. *Rev. Sci. Instrum.* **89**, 043102 (2018).

36. Shi, T., Pan, D. & Chen, J. Realization of phase locking in good-bad-cavity active optical clock. *Opt. Express* **27**, 22040–22052 (2019).

37. Elliott, G. R., Murugan, G. S., Wilkinson, J. S., Zervas, M. N. & Hewak, D. W. Chalcogenide glass microsphere laser. *Opt. Express* **18**, 26720–26727 (2010).

38. Herr, S. J., Buse, K. & Breunig, I. LED-pumped whispering-gallery laser. *Photon. Res.* **5**, B34–B38 (2017).

39. Kuehne, A. J. C. & Gather, M. C. Organic lasers: recent developments on materials, device geometries, and fabrication techniques. *Chem. Rev.* **116**, 12823–12864 (2016).

40. Huang, H. et al. Wavelength-turnable organic microring laser arrays from thermally activated delayed fluorescent emitters. *ACS Photonics* **6**, 3208–3214 (2019).

41. Metcalf, H. J. & van der Straten, P. *Laser Cooling and Trapping*. (Springer, New York, 1999).

42. Heavens, O. S. Radiative transition probabilities of the lower excited states of the alkali metals. *J. Opt. Soc. Am. B* **51**, 1058–1061 (1961).

43. Hood, C. J., Lynn, T. W., Doherty, A. C., Parkins, A. S. & Kimble, H. J. The atom-cavity microscope: single atoms bound in orbit by single photons. *Science* **287**, 1447–1453 (2000).

44. Gérard, J. M. et al. Enhanced spontaneous emission by quantum boxes in a monolithic optical microcavity. *Phys. Rev. Lett.* **81**, 1110–1113 (1998).

45. Aoki, T. et al. Observation of strong coupling between one atom and a monolithic microresonator. *Nature* **443**, 671–674 (2006).

46. Rempe, G., Thompson, R. J., Kimble, H. J. & Lalezari, R. Measurement of ultralow losses in an optical interferometer. *Opt. Lett.* **17**, 363–365 (1992).

47. Gorodetsky, M. L., Savchenkov, A. A. & Ilchenko, V. S. Ultimate Q of optical microsphere resonators. *Opt. Lett.* **21**, 453–455 (1996).

48. Gérard, J. M. et al. Quantum boxes as active probes for photonic microstructures: the pillar microcavity case. *Appl. Phys. Lett.* **69**, 449–451 (1996).

49. Akahane, Y., Asano, T., Song, B.-S. & Noda, S. High-Q photonic nanocavity in a two-dimensional photonic crystal. *Nature* **425**, 944–947 (2003).

50. Allain, P. E. et al. Optomechanical resonating probe for very high frequency sensing of atomic forces. *Nanoscale* **12**, 2939–2935 (2020).

51. Doolin, C., Kim, P. H., Hauer, B. D., MacDonald, A. J. R. & Davis, J. P. Multidimensional optomechanical cantilevers for high-frequency force sensing. *N. J. Phys.* **16**, 035001 (2014).

52. McKeown, S. J., Wang, X., Yu, X. & Goddard, L. L. Realization of palladium-based optomechanical cantilever hydrogen sensor. *Microsyst. Nanoeng.* **3**, 16087 (2017).

53. Fogliano, F. et al. Mapping the cavity optomechanical interaction with subwavelength-sized ultrasensitive nanomechanical force sensors. *Phys. Rev. X* **11**, 021009 (2021).

54. Asano, M., Zhang, G., Tawara, T., Yamaguchi, H. & Okamoto, H. Near-field cavity optomechanical coupling in a compound semiconductor nanowire. *Commun. Phys.* **3**, 230 (2020).

55. Kessler, T. et al. A sub-40-mHz-linewidth laser based on a silicon single-crystal optical cavity. *Nat. Photon* **6**, 687–692 (2012).

56. London, H., Clarke, G. R. & Mendoza, E. Osmotic pressure of He$^3$ in liquid He$^4$, with proposals for a refrigerator to work below 1°K. *Phys. Rev.* **128**, 1992–2005 (1962).

57. Bartlett, J. et al. Improved performance of an engineering model cryogen free double adiabatic demagnetization refrigerator. *Cryogenics* **50**, 582–590 (2010).

58. Scully, M. O. & Lamb, W. E. Jr. Quantum theory of an optical maser. I. General theory. *Phys. Rev.* **159**, 208–226 (1967).

59. Kolobov, M. I., Davidovich, L., Giacobino, E. & Fabre, C. Role of pumping statistics and dynamics of atomic polarization in quantum fluctuations of laser sources. *Phys. Rev. A* **47**, 1431–1446 (1993).

60. Siegman, A. E. *Lasers*. (University Science Books, 1986).

61. Kuppens, S. J. M., van Exter, M. P. & Woerdman, J. P. Quantum-limited linewidth of a bad-cavity laser. *Phys. Rev. Lett.* **72**, 3815–3818 (1994).

62. McKeever, J., Boca, A., Boozer, A. D., Buck, J. R. & Kimble, H. J. Experimental realization of a one-atom laser in the regime of strong coupling. *Nature* **425**, 268–271 (2003).

63. Dubin, F. et al. Quantum to classical transition in a single-ion laser. *Nat. Phys.* **6**, 350–353 (2010).

64. Nomura, M., Kumagai, N., Iwamoto, S., Ota, Y. & Arakawa, Y. Laser oscillation in a strongly coupled single-quantum-dot–nanocavity system. *Nat. Phys.* **6**, 279–283 (2010).

65. Jeske, J. et al. Stimulated emission from nitrogen-vacancy centres in diamond. *Nat. Commun.* **8**, 14000 (2017).

66. Vollmer, F. & Yu, D. *Optical Whispering Gallery Modes for Biosensing: From Physical Principles to Applications*. (Springer, 2020).

67. Loudon, R. Nonclassical effects in the statistical properties of light. *Rep. Prog. Phys.* **43**, 913–949 (1980).

68. Riedinger, R. et al. Non-classical correlations between single photons and phonons from a mechanical oscillator. *Nature* **530**, 313–316 (2016).

69. Yu, D. & Vollmer, F. Spontaneous PT-symmetry breaking in lasing dynamics. *Commun. Phys.* **4**, 77 (2021).

70. Kuzmich, A. et al. Generation of nonclassical photon pairs for scalable quantum communication with atomic ensembles. *Nature* **423**, 731–734 (2003).

71. Stannigel, K., Rabl, P., Sørensen, A. S., Zoller, P. & Lukin, M. D. Optomechanical transducers for long-distance quantum communication. *Phys. Rev. Lett.* **105**, 220501 (2010).

72. Diósi, L. Laser linewidth hazard in optomechanical cooling. *Phys. Rev. A* **78**, 021801 (2008).

73. Bohnet, J. et al. A steady-state superradiant laser with less than one intracavity photon. *Nature* **484**, 78–81 (2012).

74. Sandoghdar, V. et al. Very low threshold whispering-gallery-mode microsphere laser. *Phys. Rev. A* **54**, R1777–R1780 (1996).

75. Yang, L. & Vahala, K. J. Gain functionalization of silica microresonators. *Opt. Lett.* **28**, 592–594 (2003).

76. Mehrabani, S. & Armani, M. A. Blue upconversion laser based on thulium-doped silica m icrocavity. *Opt. Lett.* **38**, 4346–4349 (2013).

77. Qian, S.-X., Snow, J. B., Tzeng, H.-M. & Chang, R. K. Lasing droplets: highlighting the liquid-air interface by laser emission. *Science* **231**, 486–488 (1986).

78. Tzeng, H.-M., Wall, K. F., Long, M. B. & Chang, R. K. Laser emission from individual droplets at wavelengths corresponding to morphology-dependent resonances. *Opt. Lett.* **9**, 499–501 (1984).

79. Besga, B. et al. Polariton boxes in a tunable fiber cavity. *Phys. Rev. Appl.* **3**, 014008 (2015).

80. Prakash, G. V. et al. Tunable resonant optical microcavities by self-assembled templating. *Opt. Lett.* **29**, 1500–1502 (2004).

81. Wilson, D. J. et al. Measurement-based control of a mechanical oscillator at its thermal decoherence rate. *Nature* **524**, 325–329 (2015).

82. Anetsberger, G. et al. Near-field cavity optomechanics with nanomechanical oscillators. *Nat. Phys.* **5**, 909–914 (2009).

83. Patsyk, A., Sivan, U., Segev, M. & Bandres, M. A. Observation of branched flow of light. *Nature* **583**, 60–65 (2020).

84. D'Addabbo, A. et al. The CUORE cryostat. *J. Low. Temp. Phys.* **193**, 867–875 (2018).

85. Alduino, C. et al. The CUORE cryostat: an infrastructure for rare event searches at millikelvin temperatures. *Cryogenics* **102**, 9–21 (2019).

86. Kolkowitz, S. et al. Coherent sensing of a mechanical resonator with a single-spin qubit. *Science* **335**, 1603–1606 (2012).

87. O'Connell, A. D. et al. Quantum ground state and single-phonon control of a mechanical resonator. *Nature* **464**, 697–703 (2010).

88. Clemens, J. P., Rice, P. R. & Pedrotti, L. M. Spectra of single-atom lasers. *J. Opt. Soc. Am. B* **21**, 2025–2034 (2004).

89. Yu, D. Two coupled one-atom lasers. *J. Opt. Soc. Am. B* **33**, 797–803 (2016).

## Acknowledgements

## Author contributions

D.Y. developed all theoretical models, made the calculations, and plotted the figures. D.Y. and F.V. participated in the scientific discussion and wrote the paper.

## Competing interests

The authors declare no competing interests. F.V. is a Guest Editor of the Focus Collection "Microresonator Frequency Combs: New Horizons" in Communications Physics, but was not involved in the editorial review of, or decision to publish, this article.

## Additional information

**Supplementary information** The online version contains supplementary material available at https://doi.org/10.1038/s42005-022-00841-2.

**Correspondence** and requests for materials should be addressed to Deshui Yu or Frank Vollmer.

**Peer review information** *Communications Physics* thanks the anonymous reviewers for their contribution to the peer review of this work. Peer reviewer reports are available.

**Reprints and permission information** is available at http://www.nature.com/reprints

**Publisher's note** Springer Nature remains neutral with regard to jurisdictional claims in published maps and institutional affiliations.